Master of Science in Mechanical Engineering

Modularized Robotic Skin Sensorized by Fiber Optic Force Sensing for Remote and Autonomous Robot Operation

광섬유 힘 센서가 내장된 로봇 원격 및 무인 조작을 위한 모듈화 로봇 스킨

August 2021

Graduate School of Mechanical Engineering
Seoul National University

Sudong Lee

Modularized Robotic Skin Sensorized by Fiber Optic Force Sensing for Remote and Autonomous Robot Operation

Advisor Yong-Lae Park

Submitting a Master's thesis of
Mechanical Engineering

April 2021

Graduate School of Mechanical Engineering
Seoul National University

Sudong Lee

Confirming the master's thesis written by
Sudong Lee

June 2021

Chair	Sung-Hoon Ahn
Vice Chair	Yong-Lae Park
Examiner	Howon Lee

Abstract

Robots have been used to replace human workers for dangerous and difficult tasks that require human-like dexterity. To perform sophisticated tasks, force and tactile sensing is one of the key requirements to achieve dexterous manipulation. Robots equipped with sensitive skin that can play a role of mechanoreception in animals will be able to perform tasks with high levels of dexterity. In this research, we propose modularized robotic skin that is capable of not only localizing external contacts but also estimating the magnitudes of the contact forces. In order to acquire three pieces of key information on a contact, such as contact locations in horizontal and vertical directions and the magnitude of the force, each skin module requires three degrees of freedom in sensing. In the proposed skin, force sensing is achieved by a custom-designed triangular beam structure. A force applied to the outer surface of the skin module is transmitted to the beam structure underneath, and bending of the beam is detected by fiber optic strain sensors, called fiber Bragg gratings. The proposed skin shows resolutions of 1.45 N for force estimation and 1.85 mm and 1.91 mm for contact localization in horizontal and vertical directions, respectively. We also demonstrate applications of the proposed skin for remote and autonomous operations of commercial robotic arms equipped with an array of the skin modules.

Keyword : Modularized Robotic Skin, Tactile Sensing, Force Sensing, Fiber Optic Strain Sensing, Fiber Bragg Gratings, Remote and Autonomous Robot Operation

Student Number : 2019-23130

Table of Contents

Chapter 1. Introduction

Dexterity as high as that of humans is highly beneficial to robots for carrying out manipulation tasks in various fields [1], [2]. Robots are sometimes required to perform complex tasks in special environments that may be dangerous to humans [3], [4]. In order to deal with these situations, teleoperations [5], [6]. [7] or autonomous robotic systems with high sensing capabilities have been proposed. Force and tactile sensing is one of the essential tools in dexterous manipulation of a robot, since it not only provides spatial information on the surroundings but also enables physical feedback to the robot (i.e., mechanoreception in biology) to determine the motion when the robot interacts with the environment [8], [9]. The importance of force and tactile sensing is further emphasized in harsh environments [10] because it increases the success rate in operation while reducing the risk of damages to the robot. Therefore, researchers have been developing sensors similar to the mechanoreceptors in human or animal skin [11], [12], [13], [14], [15].

Remote operation is one area that can be directly benefited from tactile sensing, since it can effectively convey information on the locations of any contacts or on the object for manipulation. This allows the operator to quickly recognize the surroundings and to complete control tasks with dexterity. Furthermore, it helps the operator safely interact with different objects by providing information on contact forces [16]. In an autonomous system, a robot can perform sophisticated tasks stably even though it experiences unexpected collisions if the magnitudes and the locations of the contacts can be identified in real-time. This capability is highly

useful not only in performing independent tasks but also in collaborating with other robots. Therefore, we propose a new design of robotic skin that can provide real-time information on the forces and the locations of physical contacts for performing high-level manipulation tasks.

It has been well known that tactile sensing in an end-effector is one of the key requirements for dexterous manipulation [17], [18], [19]. However, that in other areas of the body is also important for the robot to be more autonomous, which can be achieved by equipping the robot with sensorized skin [12], [20]. Then, the robot will be able to quickly explore the surroundings with reduced operation time. In addition, robotic skin may increase the stability and the safety of the robot [13], even in the environments that have not been explored or keep changing. Real-time information on physical contacts helps the robot determine and modify its body configuration. Skin with tactile sensing also helps to plan the trajectory of the robot [21], [22] by providing additional information about the surroundings to visual feedback from optical systems, such as cameras or lidars [23].

There have been various research groups focusing on different types of tactile sensors for robots [13], [14], [24], [25]. However, most of them are not only difficult to estimate continuous locations of the contact force [26], but also unable to operate in harsh environments, such as areas with high electromagnetic interference (EMI) or radiation. In addition, most of them are not accurate enough in estimating the locations and the magnitudes of contact forces for dexterous manipulation.

In this paper, we propose modularized robotic skin (Figure 1) with force sensing capability achieved by fiber optic strain sensors called fiber Bragg gratings (FBGs) [27], [28] embedded in the base

layer – the sensor layer in Figure 2–a. The skin cover and the sensor layer is connected through the join layer and custom–designed joints called spherical–linear (S–L) joints that allow displacement of the skin cover with three degrees of freedom (DoFs). This three–DoF motions enables estimation of the location and the magnitude of a contact force applied to the surface of the skin.

Fiber optic sensing is a perfect solution in this application, since fiber optics are compact, flexible, and lightweight and thus easy to be embedded in a structure with a complex shape. In addition, they are immune to electromagnetic noise and radiations [29], [30], [31], making the robotic skin useful even in harsh environments. Moreover, the multiplexing capability of FBGs [32], [33], [34], [35] makes the system simple even with an increased number of sensors [31], and long distance sensing is also possible [36].

The modular design of the skin provides several advantages. First of all, it makes the skin easy to be applied to existing robotic structures with various shapes and sizes [37]. Another advantage is easy repair of the skin with failures, since it allows for partial replacement of failure modules [13], which not only reduces the repair cost but also simplifies the repair process. Finally, the modular design enables multi–touch sensing. In general, conventional robots equipped with a multi–axis force–torque sensor mostly at the wrist joint [38], [39], [40] are not able to identify multiple contacts separately. They can only process multiple forces as one representative force at the end–effector. This makes the conventional force sensing method not so practical for autonomous robots. In our approach, however, each skin module estimates the force applied to it individually, and the entire skin is able to process the information on the multiple forces simultaneously.

The prototype of our robotic skin showed resolutions of 1.85 mm and 1.91 mm for localization in lateral and longitudinal directions, respectively, and 1.45 N for force estimation. We were able to achieve a sensing bandwidth higher than 850 Hz through modeling and parameter optimization.

The rest of this paper is organized as follows. Chapter 2 describes the design concept, the key features, and the fabrication process of the skin module, followed by the design consideration for an arrayed skin structure. Chapter 3 provides modeling of the skin structure for force sensing based on the beam theory. This section also discusses continuous estimation of the locations and the magnitudes of the contact force using beam modeling results. Chapter 4 presents the result of characterization of the skin module. Chapter 5 demonstrates applications of the proposed robotic skin to remote operation and autonomous control of a robot arm. Section Chapter 6 discusses the contribution of our skin and future work, and Chapter 7 finally concludes the work.

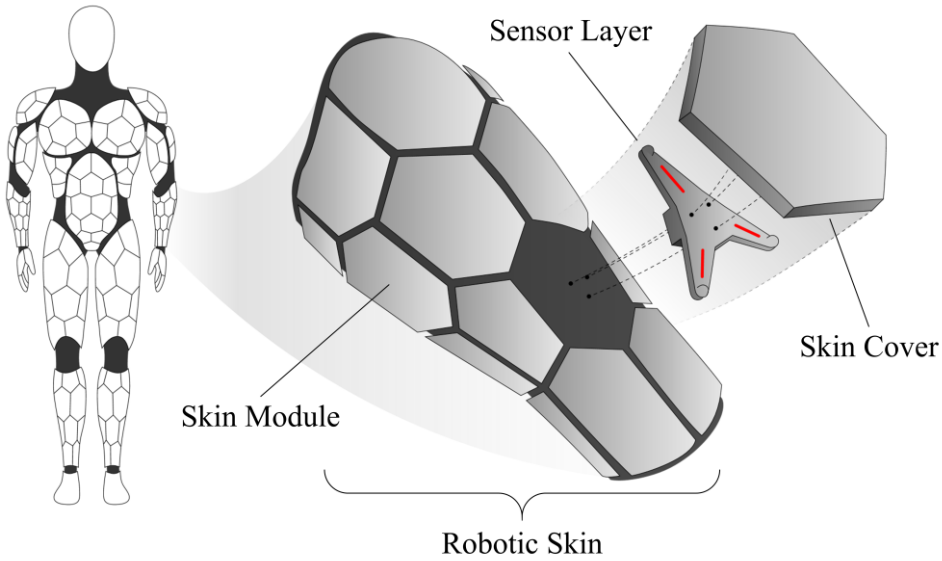

Figure 1. Conceptual drawing of modularized robotic skin composed of a skin cover and a sensing structure hidden under the cover.

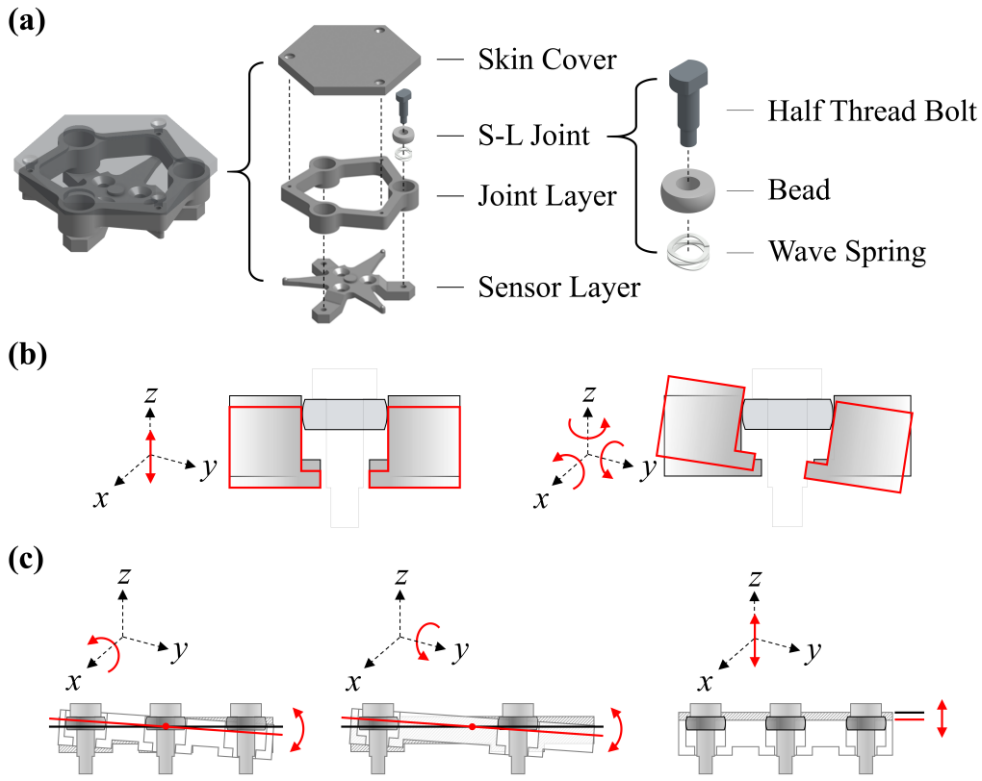

Figure 2. (a) Components of the skin module. (b) Four-DoF motions of the S-L joint. (c) Three-DoF motions in the skin module. The skin module has roll, pitch, and z-axis translation motions.

Chapter 2. Design

The robotic skin is a combination of hexagonal grids and can easily cover a curved surface. Each grid is called as a skin module in our design, and the top layer (i.e., skin cover) of each module was designed to have three-DoF motions in order to obtain three pieces of force information (the magnitude and the locations in $x-$ and $y-$ axes). The skin module consists of four components: a skin cover, a joint layer, three spherical-linear (S-L) joints, and a sensor layer.

2.1. Skin Module

1) Sensor Layer: The sensor layer is the base of the skin module, composed of a triangular beam structure and three wings with screw holes, as shown in Figure 3-a. Each beam has a small protrusion at the end, making a contact with the joint layer. A force applied to the skin cover combined with the joint layer is transmitted to the sensor layer only through these three points, and bending of the three beams allows for detection of the force with three DoFs. In other words, the strain changes of the three beams provide enough information to find out the location and the magnitude of the force. Each beam has an FBG bonded on top, which measures the strain changes of the beam, as shown in Figure 3-b. Since each FBG had its own length (approximately 3 mm) and uniform strains needed to be applied over the area where the FBG was bonded, the beam was designed to have a tapered shape. In addition to the FBGs on the beams, a fourth FBG was bonded at the center of the beam structure for temperature compensation, since the strain change at the center area was

negligible due to the three screws tightened around the center.

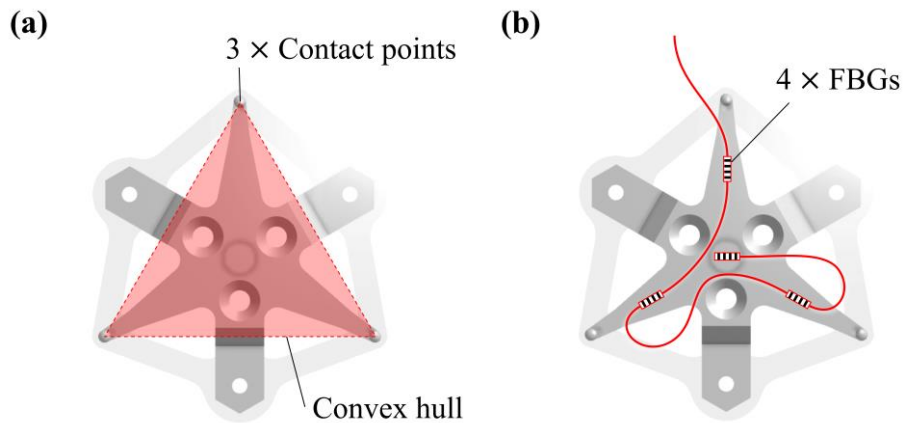

Figure 3. (a) Three contact points form the convex hull of a triangle. (b) Layout of four FBGs on the sensor layer. Three FBGs attached on the beam are for force sensing and one at the center for temperature compensation.

2) Joint Layer: The joint layer, which connects the sensor layer and the skin cover, has three cylindrical sockets. Each socket holds a S−L joint composed of a large−hole bead, a wave spring, and a half threaded bolt. The bead allows four−DoF motions of the joint layer, such as vertical translation and rotations about three axes, as shown in Figure 2−b. In order to achieve three DoFs in a skin module, three S−L joints were used at 120° intervals. Although each joint has four DoFs individually, the sensor layer fixed at the bottom constrains the yaw motion of the joint layer composed of three S−L joints. Therefore, this allowed the skin cover not only to rotate in x and y axes but also to linearly move in z−axis. Figure 2−c shows the resulting three DoFs of the skin module; roll, pitch, and vertical translation.

3) Skin Cover: The skin cover is the outermost layer of a skin module with a hexagonal shape. Hexagons are one of three types of polygons that can cover a large area without leaving gaps when arrayed, making the entire skin easily reconfigurable depending on the size or the shape of the host structure. When a force applied inside the convex hull of the sensor layer, Figure 3−a, all three corners of the triangle are compressed and causes bending of the beams. However, if the force is outside the convex hull but still in the hexagonal area, the farthest corner from the force loses the contact due to the moment about the axis that passes the other two corners. To address this issue, the sensor layer was bolted to the joint layer with prestress. In this way, the farthest beam is only relaxed from the prestress rather than losing the contact. Therefore, a force applied to anywhere inside the hexagon can be detected by the three FBGs.

4) Fabrication: All the structures and the components were made

of stainless steel by machining. The total weight of a single module is 113 g. For accuracy in sensing, both of the sensor layer and the joint layer were precisely machined to have tolerance of less than 0.01 mm. Also, the beads and the sockets of the joint layer were machined to have bearing tolerance of 0.01 mm, respectively, in order to minimize the friction. In addition, a groove (length: 4 mm) was engraved on each place for an FBG to be bonded on the joint layer using a laser cutter (Speedy 300 Flexx, Trotec, Austria). The FBGs were bonded to the grooves using cyanoacrylate adhesive, as shown in Figure 3-b.

2.2. Skin Array

To test our concept of robotic skin, we selected an industrial robot arm with cylindrical links to apply the proposed skin modules, as shown in Figure 4. The cylindrical skin structure was composed of multiple rows, and each row had six curved skin modules. The hexagonal shape of the skin cover enabled to cover the entire surface area of the arm without leaving any gaps.

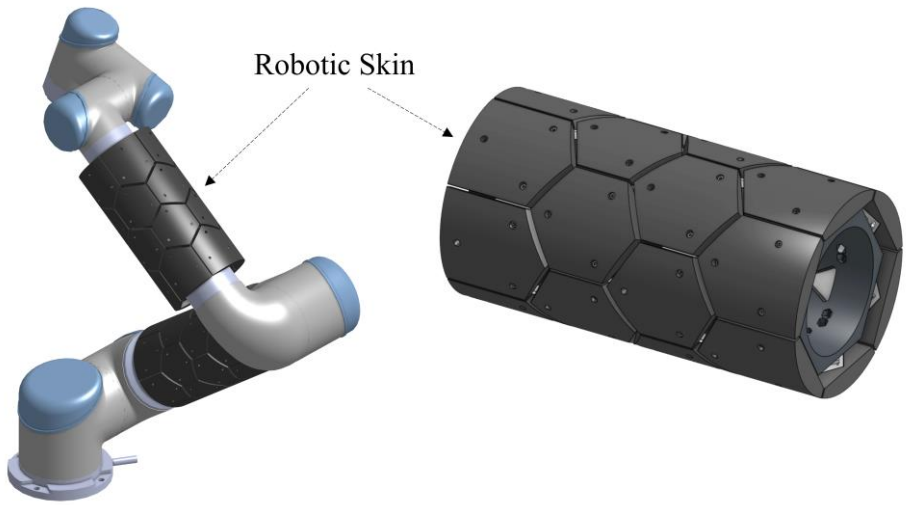

Figure 4. Industrial robot arm covered by multiple skin modules that form cylindrical skin.

Chapter 3. Modeling

3.1. FBG Sensing Principle and Temperature Compensation

When a light injected into an optical fiber meets an FBG, a specific wavelength of the input light is reflected back to the origin while the rest wavelengths are transmitted to the other side. This specific wavelength is called as a peak wavelength or a Bragg wavelength. The peak wavelength is determined by the grating pitch, Λ, and the effective refractive index, n_{eff}, of the FBG, and their relationship is [41]

$$\lambda_p = 2n_{eff} \tag{1}$$

where λ_p is the peak wavelength.

The grating pitch changes by the axial strain applied to the FBG area in the optical fiber or the temperature change of the FBG. The relative shift of the peak wavelength, $\frac{\Delta\lambda_p}{\lambda_p}$, is given as

$$\frac{\Delta\lambda_p}{\lambda_p} = (1 - p_e) \cdot \epsilon + (\alpha_\Lambda + \alpha_\eta) \cdot \Delta T \tag{2}$$

where ϵ is the strain applied to the FBG, p_e is the photo-elastic coefficient, α_Λ is the thermal expansion coefficient, α_η is the thermo-optic coefficient, and ΔT is the temperature change [42].
In order to eliminate the effect of temperature change, Equation (2) is subtracted by the relative shift of a peak wavelength that is affected not by strain but only by temperature [17].

3.2. Estimation of Beam Force and Deflection

1) Beam Modeling: The FBGs attached to the beams detect the strain changes caused by beam bending. According to the Euler–Bernoulli beam theory, the elastic curve equation of a cantilever beam in the shape of a cuboid is

$$v = \frac{-Fx^2}{6EI}(3L - x) \tag{3}$$

where v is the deflection of the beam, x is the horizontal location in the beam, F is the load, E is the Young's modulus, I is the moment of inertia of the cross-sectional area about the neutral axis, and L is the horizontal length of the beam [43]. This equation can be simplified at $x = L$ as

$$v = \frac{-FL^2}{3EI}. \tag{4}$$

The differential equation about x in this system is given as

$$\frac{dv}{dx} = \frac{-F}{2EI}(2Lx - x^2). \tag{5}$$

Based on the above equations, the beam does not experience uniform strains along its length. However, FBGs have their own lengths, and it will be highly useful if uniform strains can be applied at least to the area to which an FBG is bonded. This will not only reduce the computational cost but also increase the accuracy in strain measurement. Moreover, we do not need to use any special calibration process to find a nominal strain of a section [44]. Therefore, we designed a tapered beam. Figure 5-a compares the strain uniformities of a regular beam and a tapered beam.

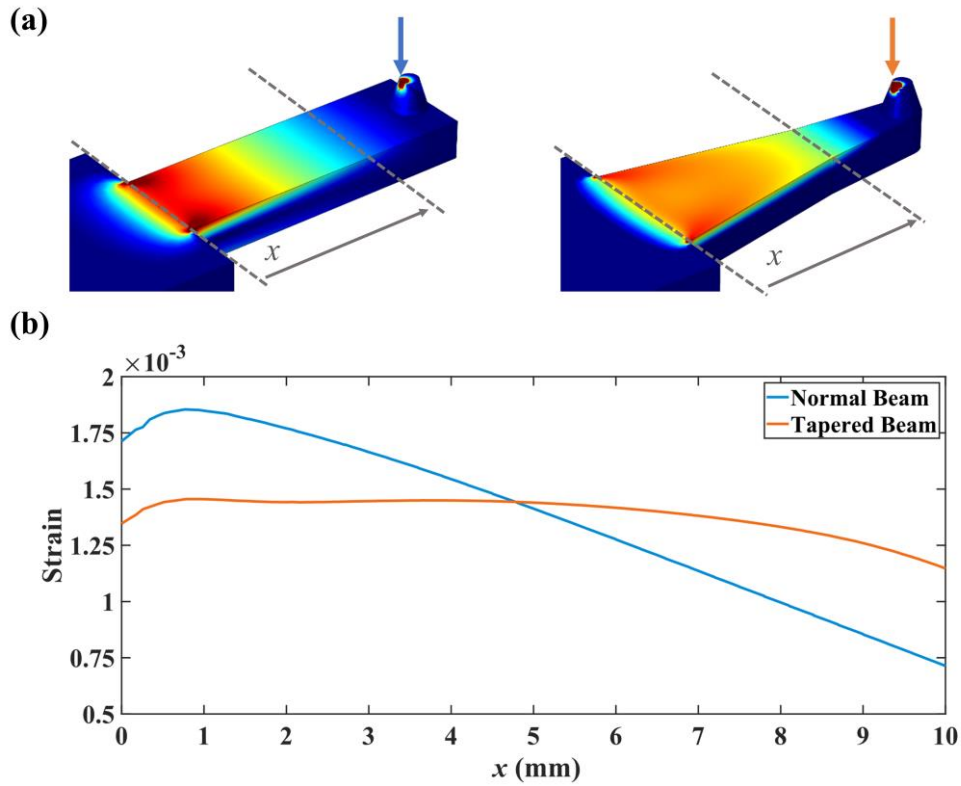

Figure 5. Comparison of strain profiles of a regular beam and a tapered beam. The strain at the top surface of the regular beam decreases linearly along the length while that of the tapered beam maintains relatively constant. (a) Graphical comparison. (b) Quantitative comparison.

The flexure formula is given as

$$\sigma = E\epsilon = \frac{My}{I}, \qquad I = \frac{bh^3}{12}, \qquad y = \frac{h}{2} \tag{6}$$

where σ is the normal stress about the cross-sectional area, ϵ is the strain, y is the vertical distance from the neutral axis, M is the internal moment about the neutral axis, b is the width, and h is the height of the cross-section area [43]. Since M is equal to $F(x-L)$, Equation (6) can be expressed as

$$\epsilon = \frac{My}{EI} = \frac{6F(x-L)}{Ebh^2}. \tag{7}$$

If we choose $b = m(L-x)$ or $h = n\sqrt{L-x}$ where m and n are arbitrary real numbers, the strain, ϵ , is independent of x. Since the flat top surface is easy to bond an FBG, we choose $b = m(L-x)$, and the strain can be found from the following relationships:

$$F = \frac{mEh^2}{6}\epsilon = K_b\epsilon, \qquad K_b = \frac{mEh^2}{6} \tag{8}$$

where K_b is the proportional constant of the beam between the strain and the external force. We checked the tapered beam design using a finite element analysis (FEA) (COMSOL Multiphysics, Comsol), as shown in Figure 5. When the same force is applied to the beams of the same length. The strain of the regular beam decreased linearly along the length while that of the tapered beam showed much more uniform. According to the strain equation, $F = K_b\epsilon$, the strain curve should be completely flat, but the FEA result shows slight decrease toward the end. This is because there is stress concentration at the base of the beam and the width is not $m(L-x)$ at the tip that makes a contact with the joint layer.

The beam deflection for the applied force has a linear relationship as follows (as seen in Equation. (31) in Chapter 8. Appendix)

$$v = K_v F \quad (9)$$

where v and K_v are the deflection and the deflection proportional constant, respectively.

2) Experimental Verification of Beam: According to the FEA simulation result, the strain curve was not a completely flat curve, meaning K_b was not constant along the length of the beam. In order to experimentally verify the simulation result, a beam bending test was conducted.

We applied a force to a tapered beam with an FBG bonded using a motorized stage, and the compression force was measured by a load cell. The relationship between the force and the peak wavelength shift was linear, as shown in Figure 6-a. After updating the Young's modulus of the material in simulation with the one found in the experiment, the results from the simulation and the experiment well matched. The linear fits of the two results were almost identical.

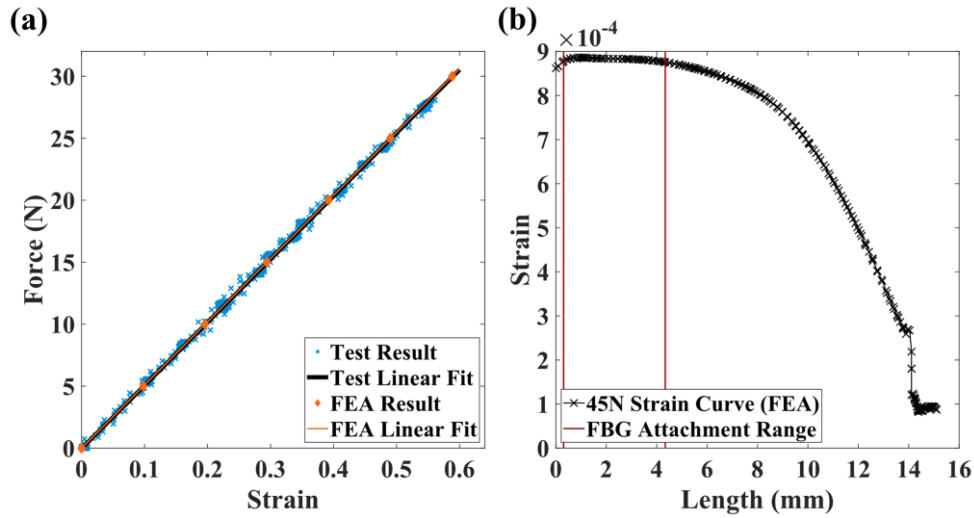

Figure 6. (a) Comparison between the experimental and the FEA results. The FEA result using the modified Young's modulus is almost identical with the experimental result. Both results show that force is linearly proportional to strain. (b) Strain profile of the tapered beam along the length when a tip force of 45 N was applied. The difference between the maximum and the minimum strains is less than 1.2×10^{-5} between 0.30 mm and 4.34 mm (two red lines).

3) Beam Parameters: The maximum sensing force of each beam in our design is 45 N, which was determined by the maximum stress concentrated at the boundary before yielding, based on the FEA result. We can also estimate the minimum sensing force of each beam 0.62 N, considering the noise level of the FBG interrogator (SI255, Micron Optics, USA), approximately 1.2×10^{-2} nm, which corresponds to 1.2×10^{-5} strain. Each beam is designed to be long enough to hold an FBG of 3 mm. The difference between the maximum and the minimum strains of the section for an FBG should be 1.2×10^{-5} or smaller at 45 N considering the accuracy of the interrogator. Figure 6−b shows the strain curve and the possible FBG area for attachment at a tip force of 45 N. The length of the possible area is 4.04 mm, and the difference between the maximum and the minimum strains is 1.1×10^{-5} strain. 4 mm is a sufficient length for attachment of an FBG of 3 mm, considering manufacturing tolerances.

3.3. Estimation of Spring Force

When a force is applied to the skin cover, the three beams in the sensor layer bend while maintaining the contacts with the joint layer. The three contact points between the beams and the joint layer constitute a beam plane, as shown in Figure 7−a. Since the FBG outputs tell the state of beam bending, the positions of the three contact points can be obtained using Equation (9). Then, the normal vector of the beam plane is

$$\left(\overrightarrow{P_{beam_2}}-\overrightarrow{P_{beam_1}}\right)\times\left(\overrightarrow{P_{beam_1}}-\overrightarrow{P_{beam_3}}\right)=\overrightarrow{N_{beam}} \qquad (10)$$

where $\overrightarrow{P_{beam_1}}$, $\overrightarrow{P_{beam_2}}$, and $\overrightarrow{P_{beam_3}}$ are the position vectors of the contact points, and $\overrightarrow{N_{beam}}$ is the normal vector of the inner plane.

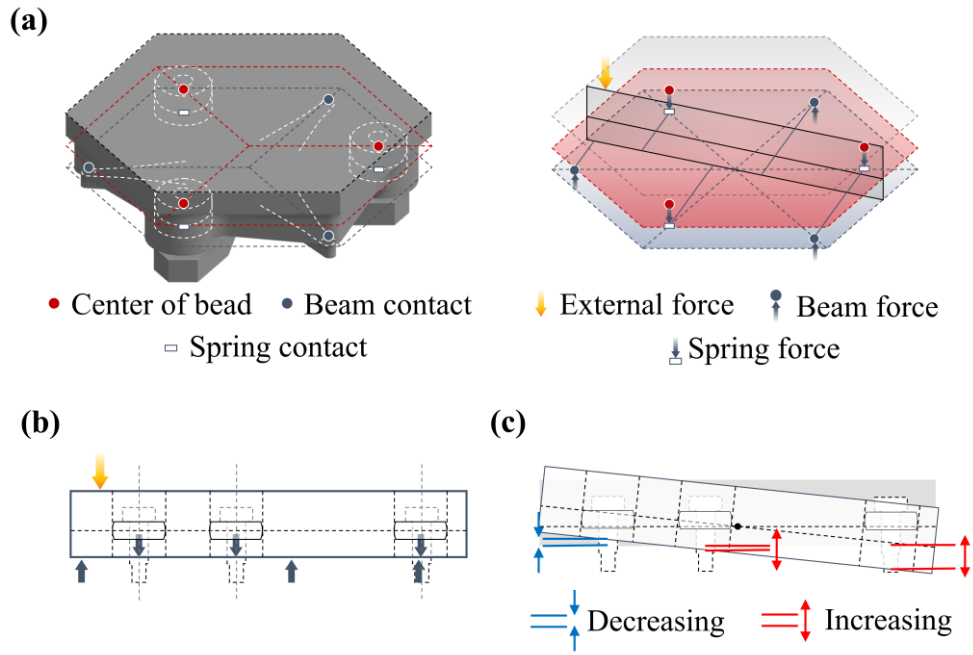

Figure 7. Model of the skin module. (a) Free body diagram of the joint layer and the skin cover. cross-sectional plane (black solid line) is formed by the center of the skin module and the external force. (b) Free body diagram of the cross-sectional plane. (c) Deformed shape of the module on the cross-sectional plane showing the displacements of the three springs in the S-L joints.

The equation of the beam plane is determined by the position of the first beam contact point as

$$\overrightarrow{N_{beam}} \cdot \left(\vec{p} - \overrightarrow{P_{beam_1}}\right) = 0 \quad (11)$$

where $\vec{p}$ is an arbitrary point of the beam plane. The initial position of the bead in each S-L joint is constrained by the wave spring and the bolt head of the joint. When a force is applied to the center of the skin cover, the beads are located below the bolt heads because the joint layer moves down horizontally. If the force is applied to anywhere on the cover except for the center, the joint layer is tilted, as shown in Figure 7-c. Since the prestressed springs always push the beads upwards and the beads are manufactured to have bearing tolerances with the sockets, the beads remain in the same positions. Therefore, the initial bead positions below the bolt heads can be maintained. The vertical displacement of the beam plane corresponds to the length changes of the springs in the equation for x and y positions, which can also be related to the changes of the spring forces, $\Delta\overrightarrow{F_{spring,i}}$ for $i = 1,2,3$.

The beam plane equation can be used to find the x, y positions where the spring and the joint layer meet because the bolts constrain the x, y positions of each spring. These positions are expressed as $\overrightarrow{P_{spring,i}}$ for $i = 1,2,3$.

3.4. Estimation of Contact Locations and Force

1) Flat Skin Cover: We assume that the external contact force is applied perpendicular to the surface of the skin cover and the shear force is thus negligible. Figure 7-b shows the configuration of the external force, the beam forces, and the spring forces in each skin module. The beam forces can be obtained by Equation (8), and

prestressed beam forces can also be obtained. Since the skin module needs to achieve a static equilibrium, the sum of the spring force changes and the beam force changes becomes the magnitude of the external force. We can now estimate the magnitude and the location of the external force using a force balance equation and a moment balance equation. The force balance equation is given as

$$\overrightarrow{F_{external}} + \sum_{i=1}^{3} \Delta\overrightarrow{F_{beam,i}} + \sum_{i=1}^{3} \Delta\overrightarrow{F_{spring,i}} = 0 \tag{12}$$

where $\overrightarrow{F_{external}}$ is the external forces, $\Delta\overrightarrow{F_{beam,i}}$ is the change of each beam force. The moment balance equation is then

$$\begin{aligned}\left(\overrightarrow{P_{external}} \times \overrightarrow{F_{external}}\right) + \sum_{i=1}^{3} \left(\overrightarrow{P_{beam,i}} \times \Delta\overrightarrow{F_{beam,i}}\right) \\ + \sum_{i=1}^{3} \left(\overrightarrow{P_{spring,i}} \times \Delta\overrightarrow{F_{spring,i}}\right) = 0\end{aligned} \tag{13}$$

where $\overrightarrow{P_{external}}$ is the location of the external force.

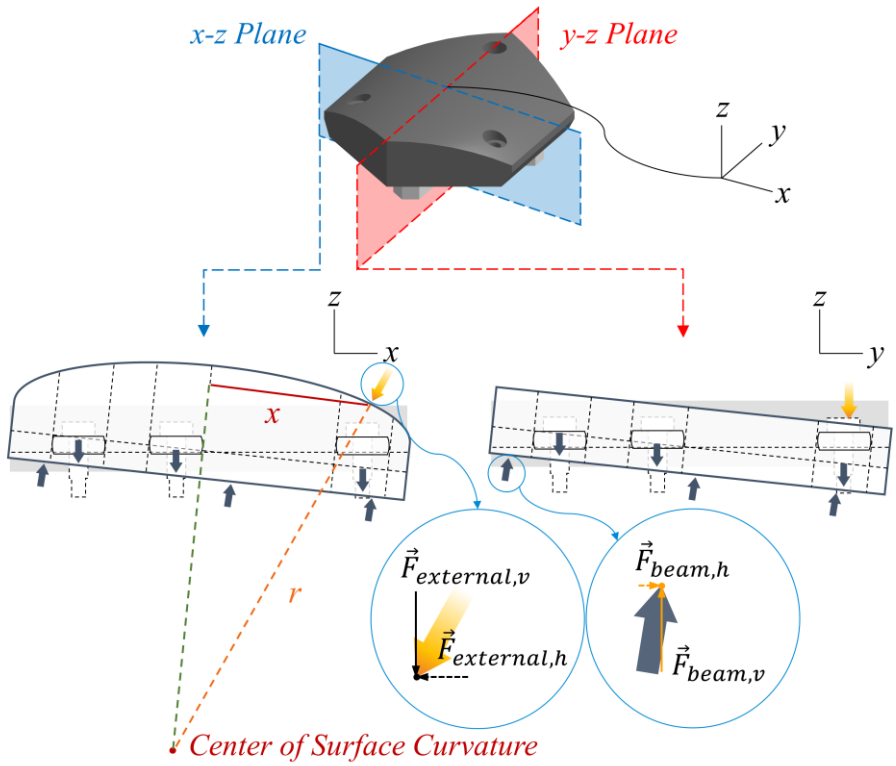

Figure 8. Model of the curved surface skin module. The left is for $x-z$ plane, and the right is for $y-z$ plane. x is the location of the force in $x-$axis, and r is the radius of the surface curvature.

2) Curved Skin Cover: In the same way as the flat skin cover modeling, we assume that the external force is perpendicular to the surface of the skin cover and that the shear force is negligible due to the low surface friction. However, it is necessary to consider the surface shape of the skin cover in modeling. To solve this problem, a geometric constraint and additional forces are added to the model.

The difference in modeling for a curved surface from that for a flat one is that the external force has a lateral component to make the force perpendicular to the surface of the skin cover. The skin cover is curved only about $y-$axis, assuming it covers a cylindrical robotic structure whose axis is parallel with $y-$axis, as shown in Figure 8. Thus, the force is composed of only $x-z$ components.

According to Figure 8, the magnitude of the horizontal component of the force and the force vector are given as

$$\begin{aligned} \left|\overrightarrow{F_{external,h}}\right| &= \left|\frac{x}{\sqrt{r^2-x^2}}\overrightarrow{F_{External,v}}\right|, \\ F_{external} &= \overrightarrow{F_{external,v}} + \overrightarrow{F_{external,h}} \end{aligned} \tag{14}$$

where $\overrightarrow{F_{external,h}}$ is the horizontal component of the beam force, x is the location of the force in $x-$axis, and r is the radius of the surface curvature, which is the same as the radius of the cylindrical robotic skin.

We assume that the S-L joints apply forces to the beams perpendicular to the beam plane. According to Figure 8, the beam force is given as

$$\overrightarrow{F_{beam}} = \frac{\left|\overrightarrow{F_{beam,v}}\right|^2}{\overrightarrow{F_{beam,v}} \cdot \overrightarrow{N_{beam}}}\overrightarrow{N_{beam}} \tag{15}$$

where $\overrightarrow{F_{beam,v}}$ is the vertical component of the beam force, and $\overrightarrow{N_{beam}}$ is the normal vector of the beam plane.

$\overrightarrow{F_{beam,v}}$ and $\overrightarrow{N_{beam}}$ can be calculated from Equation (8) and

Equation (10) , respectively. $\overrightarrow{F_{spring,v}}$ is obtained in the same way as the flat surface modeling. Finally, $\overrightarrow{F_{external,v}}$ is given as

$$\overrightarrow{F_{external,v}} + \sum_{i=1}^{3} \Delta\overrightarrow{F_{beam,i}} + \sum_{i=1}^{3} \Delta\overrightarrow{F_{spring,i}} = 0 . \qquad (16)$$

Since the moment balance equation is equal to Equation (13), we can finally find the magnitude and the location of the contact force by solving Equation (13) and (14).

Chapter 4. Experiments

We conducted experiments to characterize the proposed system by applying forces to various locations on the skin cover. The estimated magnitude and the locations of the forces were compared with the reference values. Parameter optimization was also conducted to increase the estimation accuracy.

4.1. Experimental Setup

Figure 9-a shows the setup for experiments. An indentor was combined with a load cell (RFT60-HA01, Robotous, Korea) and attached to a motorized $x-y-z$ table. Forces were applied to the skin cover by the indenter. Figure 9-b shows the system configuration and the data flow. The FBG data were collected by the interrogator, and the reference force data were measured by the load cell. The position commands for the $x-y-z$ table were used as the reference location of the force.

For the experiments, forces were applied to the entire area of the skin cover every 2 mm in both x and y axes with a grid pattern, as shown in Figure 9-c. The grid did not include the areas for bolts fixing the skin cover. The force at each location was continuously increased up to the limit and decreased back for collecting train data. Additional data were obtained independently by applying external forces to random locations for collecting test data, as shown in Figure 9-d. The train data were used for parameter optimization, and the test data were used to evaluate the result of the optimization.

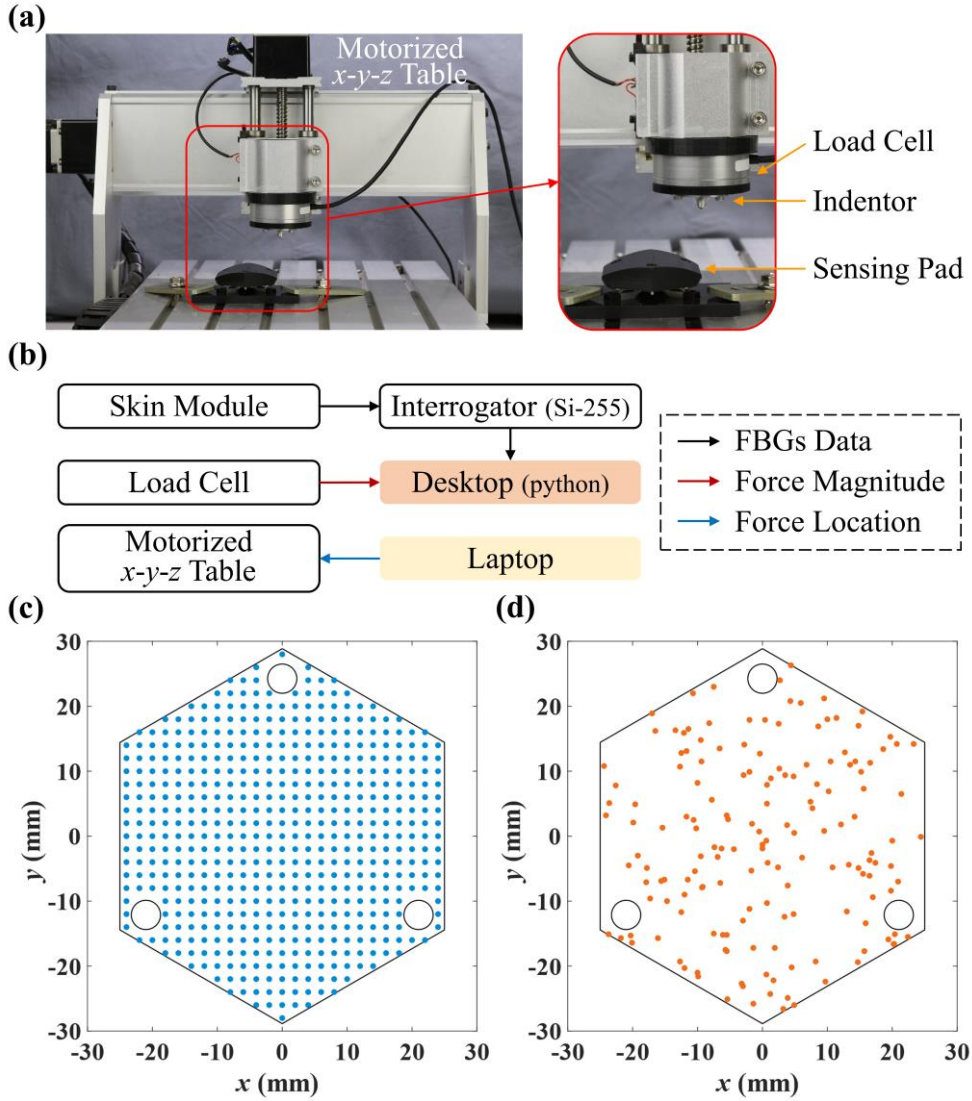

Figure 9. (a) Experimental setup. (b) System configuration and data flow. (c) Train data and (d) test data of force locations on the skin cover.

4.2. Initialization

Since the FBG peak wavelength may change depending on the external environment, such as temperature. It is necessary to initialize the sensor outputs at the start of sensing , which can be done by simply subtracting the offset from the outputs. The average of the first 60 FBG data before applying external forces was used to determine the offset value. By processing the data through modeling, the offset values that make the external force closest to zero were numerically obtained.

4.3. Parameter Optimization

Although we assumed a frictionless condition in modeling, there was actually friction in the S-L joints of the prototype, which prevented full transmission of the force applied to the skin cover to the sensor layer. Therefore, it was necessary to optimize the constants, K_b and K_v, for accurate estimation of the magnitude and position of the beam forces.

The initial values of optimization were obtained by directly applying the forces to the three beams without the skin cover and the joint layer. The constants were optimized using nonlinear least squares method to minimize the difference between the reference and the collected data at 2mm intervals. Since the skin module was asymmetric about the x-axis, K_b and K_v values for each beam were optimized. As a result, K_b and K_v were changed by 21.11 % and 36.49 % in average, respectively.

4.4. Result

1) Flat Skin Cover: Figure 10-a,b,c shows part of the experimental results of estimating the locations and the magnitude of forces applied to the skin cover based on the beam model and the optimized K_b and K_v. The RMSEs for estimating the x and y locations were 1.85 mm and 1.91 mm, respectively. The RMSE for estimating the magnitudes was 1.45 N. The RMSE for increased forces of every 5 N is plotted in Figure 10-d. When the magnitude of the force is low (near zero), the accuracy of the location is relatively low. This is because the signal to noise ratio was small in the small force range, and the skin module did not completely return to the initial position due to the friction. The RMSE for increased forces of every 5 mm from the origin is as shown in Figure 10-e. When the noise range of the raw data was removed, the minimum estimated force based on the modeling was 4.3 N. When the force based on the modeling result is between 4.3 N and 4.35 N, the average of the reference forces is 2.10 N, and this value is the actual minimum force that the sensor can detect.

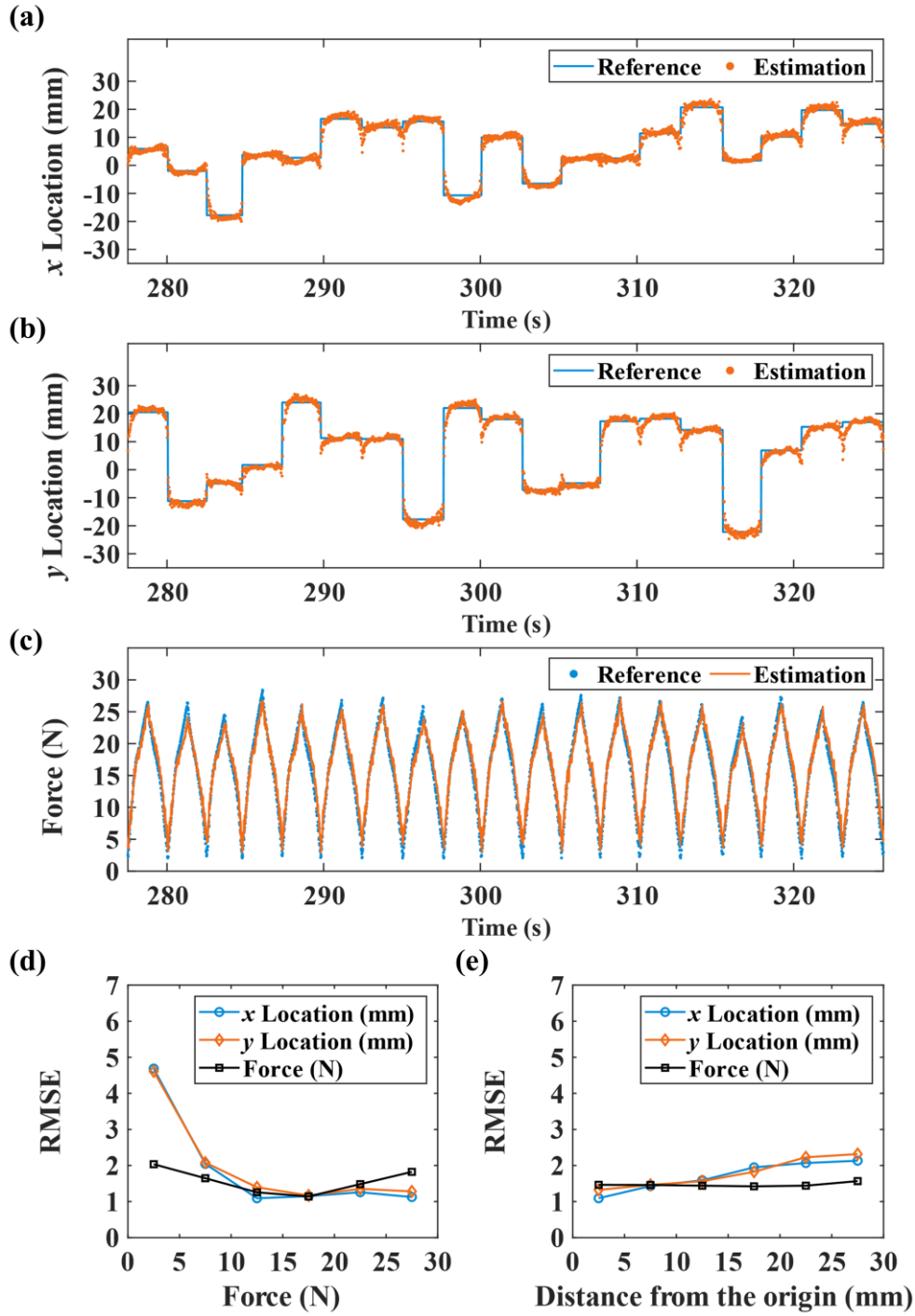

Figure 10. Part of the experimental results for estimating locations in (a) x−axis and (b) y−axis and (c) magnitudes of forces applied to the flat skin cover. RMSE values (d) for every 5 N of applied force and (e) for every 5 mm from the origin.

2) Curved Skin Cover: We also conducted an experiment for the curved skin cover in the same way for the flat skin cover. Figure 11-a,b,c shows the results of estimating the locations and the magnitude of forces based on the model of the curved surface and the optimized K_b and K_v. The RMSEs for estimating the x and y locations were 1.80 mm and 1.67 mm, respectively. The RMSE for the magnitude was 1.74 N. The RMSE for every 5 N of applied force is shown in Figure 11-d. When the magnitude of the force is low, the accuracy is relatively low, similar to the result of the flat skin cover. Since the correction for the lateral component of the external force was not perfect, the RMSE for magnitude estimation was relatively high. The RMSE for estimating the locations every 5 mm from the origin is shown in Figure 11-e.

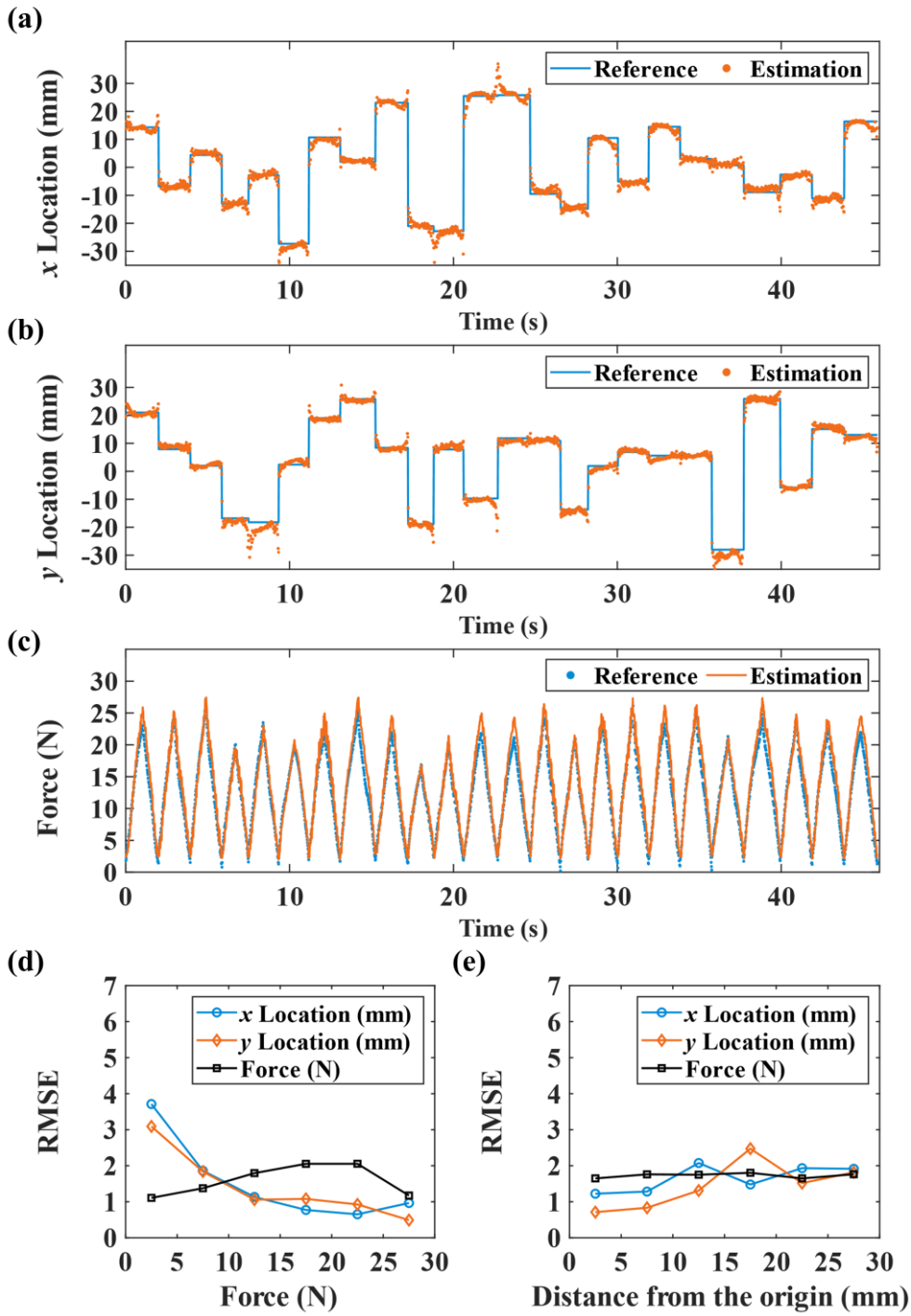

Figure 11. Part of the experimental results for estimating locations in (a) x−axis and (b) y−axis and (c) magnitudes of forces applied to the curved skin cover. RMSE values (d) for every 5 N of applied force and (e) for every 5 mm from the origin.

Chapter 5. Application

We demonstrate two application areas where the proposed robotic skin can be effective on improving the performance: remote manipulation and autonomous control of robots.

5.1. Remote Robot Manipulation

The robotic skin was mounted on a robotic arm close to the end-effector, and the arm was controlled by a human operator using a haptic feedback device. The user was asked to move the robot by manipulating the haptic device. When the robot makes a contact with an unknown object, the information on the contact force was provided to the operator through the force feedback of the haptic device. We conducted two experiments in this demonstration: shape tracing of an unknown object and path finding with obstacle avoidance. During the experiments, force feedback was the only information that was provided to the operator in real-time.

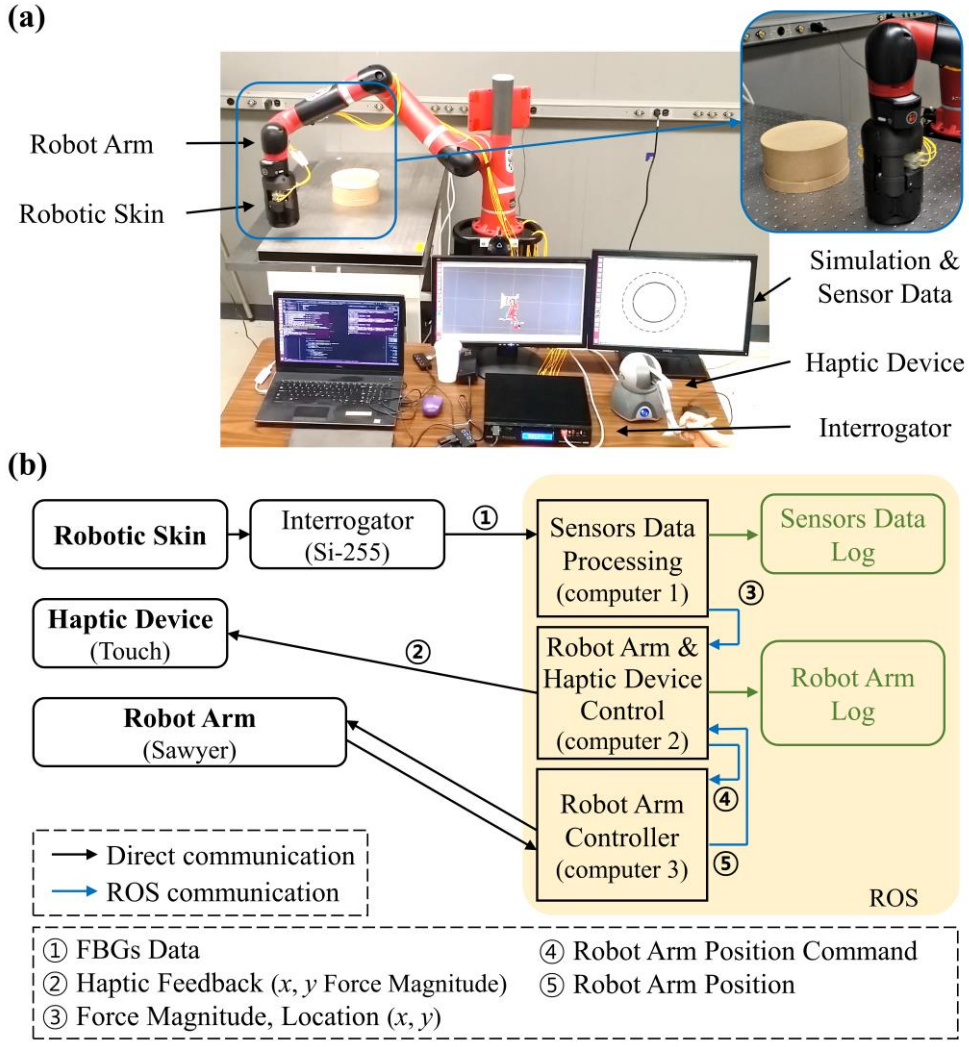

Figure 12. (a) Robot arm and operator setup for shape tracing by remote robot manipulation. The robot arm, the haptic device, and the interrogator are, respectively, connected to each computer. (b) System configuration and data flow for shape tracing by remote robot manipulation.

1) Shape Tracing: The skin was mounted on a robotic arm (Sawyer, Rethink Robotics GmbH, Germany) that was controlled by a haptic device (Touch, 3D Systems, USA), as shown in Figure 12. The operator was asked to start the experiment by moving the robot arm straight forward using the manipulator of the haptic device. As soon as the robot touches an object fixed on the ground, the operator feels the contact through force feedback. Then, the operator was asked to detour the object maintaining the contact. If the operator applies too large force to the object, it is hard to detour it. If the force is too small, it is easy to lose the contact. This task was possible, since the end of the arm was surrounded by the skin that can detect both the magnitude and the location of the contact force. The operator was able to maintain the contact during the experiment, as shown in Figure 13. The average force applied to the object was 12.43 N with a standard deviation of 5.59 N.

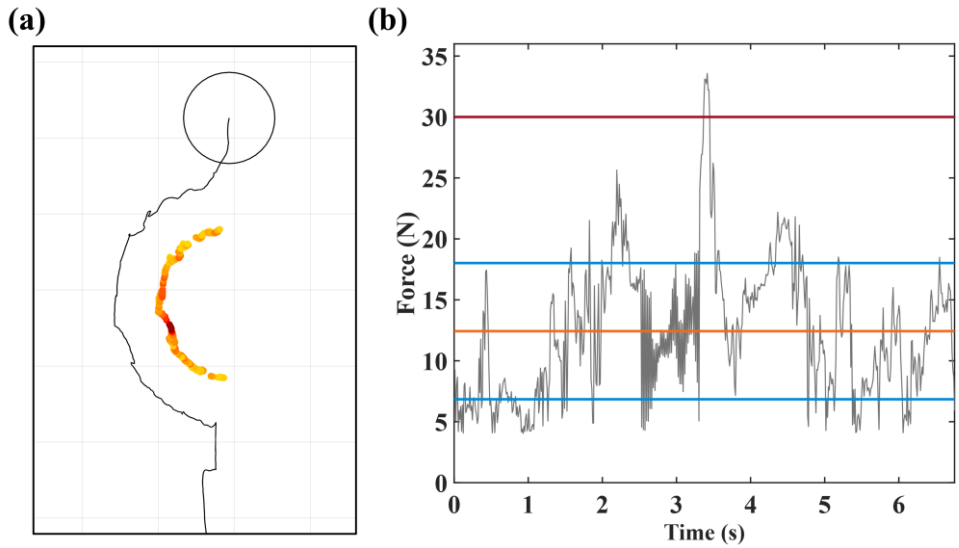

Figure 13. Shape tracing results with haptic device. (a) Position result. The black line is the robot arm path, and the black circle is current position of the robot arm. The yellow to red dots are the location where the force is applied, and color of the dot is the closer to red, the closer to 30 N. (b) Force result when the forces are applied the robotic skin. The red line is limitation of the force, the orange line is the average force, and the blue line is the range of the standard deviation.

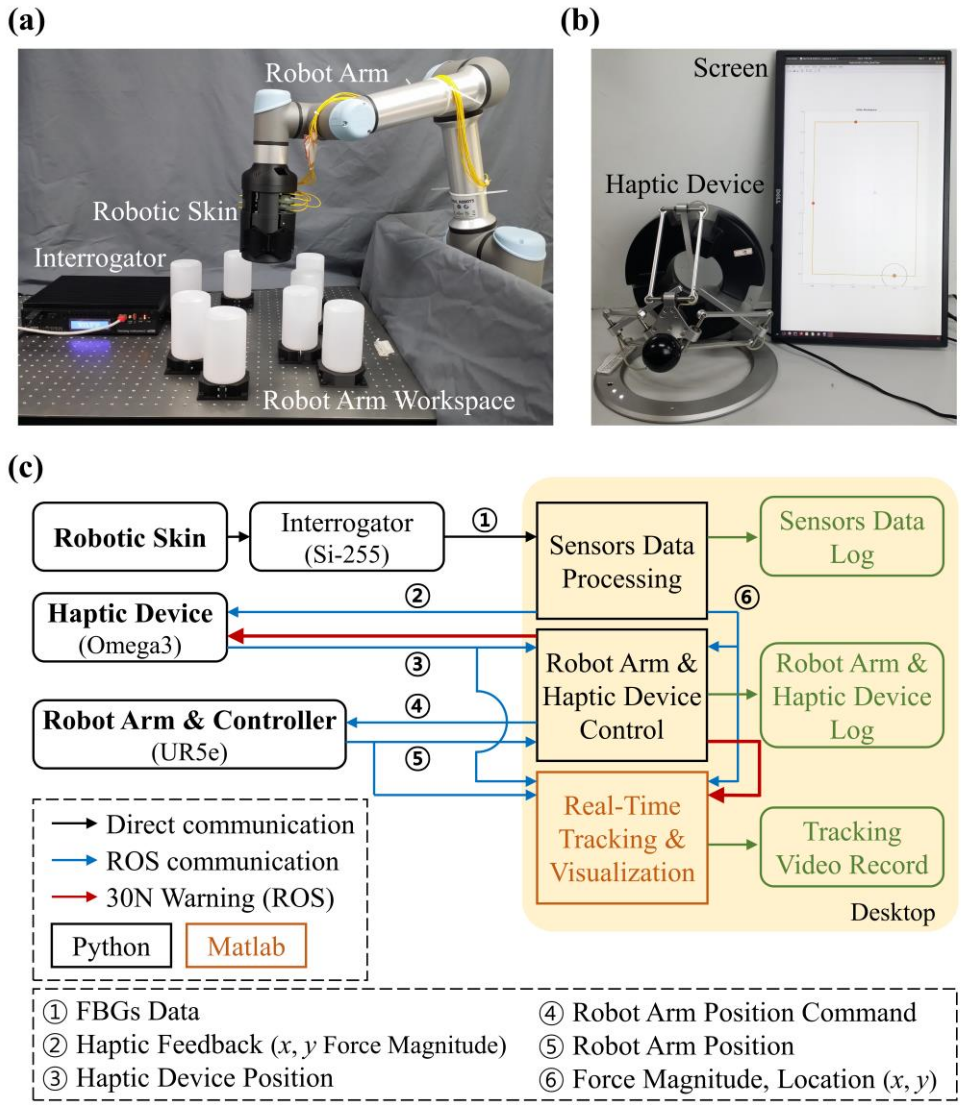
(a)
Robot Arm
Robotic Skin
Interrogator
Robot Arm Workspace
(b)
Screen
Haptic Device
(c)
Robotic Skin
Interrogator (Si-255)
①
Sensors Data Processing
Sensors Data Log
②
⑥
Haptic Device (Omega3)
③
Robot Arm & Haptic Device Control
Robot Arm & Haptic Device Log
④
Robot Arm & Controller (UR5e)
⑤
Real-Time Tracking & Visualization
Tracking Video Record
Desktop
Direct communication
ROS communication
30N Warning (ROS)
Python
Matlab
① FBGs Data
② Haptic Feedback (x, y Force Magnitude)
③ Haptic Device Position
④ Robot Arm Position Command
⑤ Robot Arm Position
⑥ Force Magnitude, Location (x, y)
(d)
(e)
Rotating Object
Fixed Object

Figure 14. (a) Robot arm setup. The robot arm and the interrogator are, respectively, connected to the computer using the LAN communication. (b) Operator setup. (c) System configuration and data flow. (d) Multi obstacles for path finding experiment with obstacle avoidance (Experimental setup). This setup was used in remote robot manipulation and in autonomous robot control. (e) Objects for object manipulation experiment through force control (Experimental setup). This setup was used in autonomous robot control.

2) Path Finding with Obstacle Avoidance: The next experiment is extension of the previous one by increasing the number of the objects and the travel complexity of the robot. The skin was mounted on an industrial robot arm (UR5, Universal Robots, Denmark) that was controlled by a haptic device (Omega3, Force Dimension, Switzerland), as shown in Figure 14. In this experiment, the operator was asked to move the robot to two waypoints one after the other and to return to the starting location. Before starting the experiment, the operator has information only on the initial position of the robot and the locations of the two waypoints on a map (Figure 15-a). As soon as the robot moves, the trajectory of the robot and the contact information of the obstacles up to the current position are provided on the screen. The operator feels the contact force during the experiment through the force feedback of the haptic device. The operator was able to complete the task even with multiple obstacles using the contact information provided by the skin, as shown in Figure 15. The average force applied to the obstacles during the experiment was 9.23 N with a standard deviation of 4.35 N.

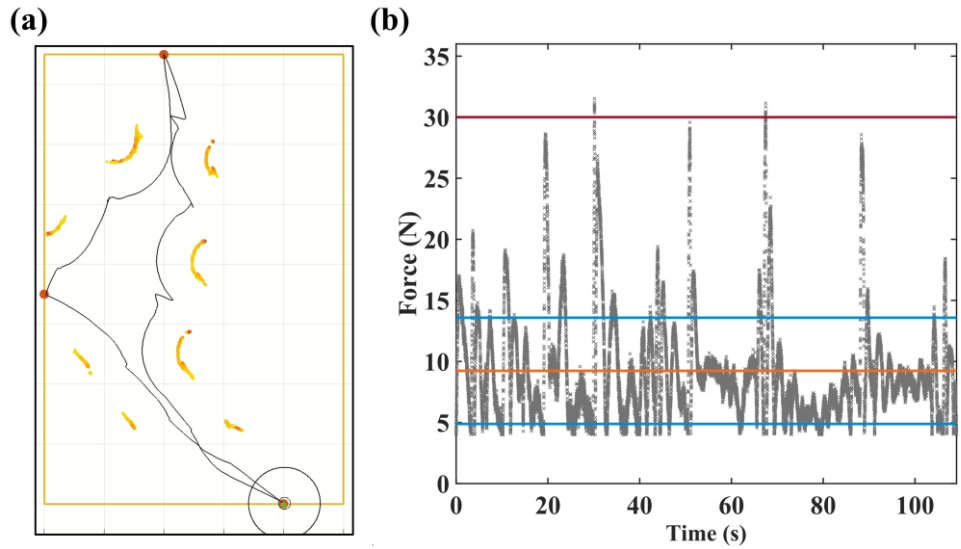

Figure 15. Path finding results with obstacle avoidance by remote robot manipulation. (a) Position result. The large brown dots are target points. Other expressions are the same as Figure 13-a. (b) Force result when the forces are applied the robotic skin. The expression method is the same as Figure 13-b.

5.2. Autonomous Robot Control

In this application, we demonstrate the performance of autonomous robot control using the proposed skin system. We conducted two experiments: path finding with obstacle avoidance and manipulation of a free-moving object through force control.

1) Path Finding with Obstacle Avoidance: The second experiment in Chapter 5.1 was conducted with a human operator. However, in this experiment, the robot operated without a human. The robot travels passing two waypoints and returns to the starting point avoiding obstacles autonomously. The initial path of the robot was given only by straight lines that connect the origin and the waypoints. However, if the robot meets obstacles, it autonomously avoids them while trying to keep the original trajectory as much as possible. The robot was successfully complete the task, as shown in Figure 16. The average force applied to the obstacles during the experiment was 7.46 N with a standard deviation of 2.67 N.

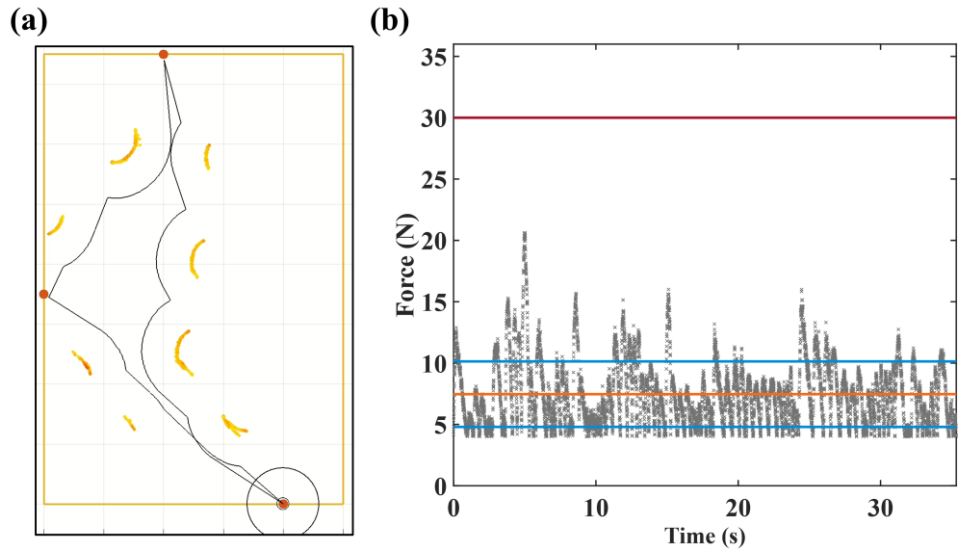

Figure 16. Path finding results with obstacle avoidance by autonomous robot control. (a) Position result. The large brown dots are target points. Other expressions are the same as Figure 13-a. (b) Force result when the forces are applied the robotic skin. The expression method is the same as Figure 13-b.

2) Object Manipulation through Force Control: Manipulation of a free-moving object requires a combination of detection of the contact location and sensing of the contact force of the target object, which can be enabled by our robotic skin. In this experiment, two same-sized cylindrical objects were prepared. One was fixed on the ground and the other object can move freely around the first object. In this task, the robot was ordered to rotate the second cylinder around the first one while maintaining the contact and controlling the contact force. The contact location on the robot continuously changes during rotation, but a constant contact force needs to be applied even with the continuous change of the contact location.

The proportional–integral–derivative (PID) controller was used to control the contact force. A mass-spring model was used for the force control, which is expressed with

$$m\ddot{x} + K_s x = f \tag{17}$$

where m is the mass, $\mathrm{K_s}$ is the spring constant, and f is the applied force by the robot arm. The PID controller applied to f is [45]

$$f = K_p x_e + K_i \int x_e dt + K_d \dot{x_e}, \qquad x_e = x_d - x \tag{18}$$

where $\mathrm{K_p}$, K_i , K_d, K_e and x_d are, respectively, the proportional gain, the integral gain, the derivative gain, the position error, and desired position. Since the mass-spring system is also applied to the object, and we assume the object is static, the contact force equation for the object is

$$f = m'\ddot{x} + K_s' x = K_s' x \tag{19}$$

where f is the contact force which is the same as the applied force by the robot, $\mathrm{m'}$ is mass of the object, and $\mathrm{K_s'}$ is spring constant of the object. Using Equation (18) and Equation (19), the f is given as

$$f = \frac{1}{K_s'}\left(K_p f_e + K_i \int f_e dt + K_d \dot{f_e}\right), \qquad f_e = f_d - f \tag{20}$$

where f_e is the force error, and f_d is desired force. The equation for the position can be converted to the equation for the force, and we can include the measured force in the controller.

Then the force equation in our application is

$$d - \frac{f_{next}}{K_s'} = \left[\left(d - \frac{f_{current}}{K_s'} + \frac{f}{K_s'}\right)^2 + L^2\right]^{0.5} \quad (21)$$

where d is the distance from the center of the fixed cylinder to the contact position, f_{next} is the applied force in the next step, f_{curent} is the applied force in the current step, and L is the travel distance in the direction perpendicular to the force. This equation is a combination of the mass-spring system and the geometric constraints. The block diagram of the controller used in our experiment is shown in Figure 17.

During the experiment, the robot rotated the free-moving cylinder around the fixed one counterclockwise first and returned it to the original location by rotating it clockwise. The target force is 6 N, and the result is shown as Figure 18. The average force applied to the object was 6.04 N with an RMSE of 0.64 N. The robotic skin allowed the robot to control the contact force on the surface of the arm autonomously even with the change of the position.

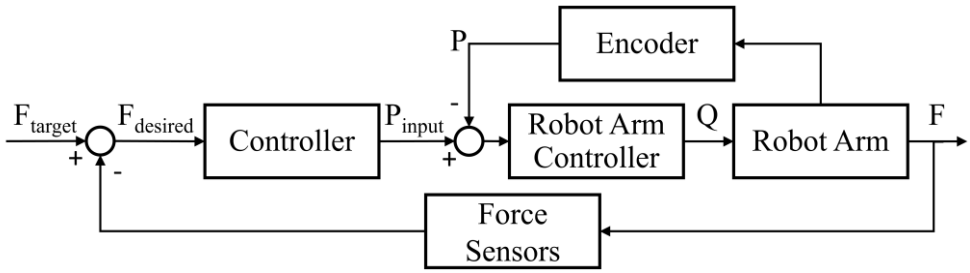

Figure 17. Position-based force-control block diagram. F_{target} is the target contact force and F is the contact force.P_{input}, $P_{desired}$, and P are, respectively, the input command end-effector position, the desired end-effector position, and the end-effector position. Q is the input commands of each joint.

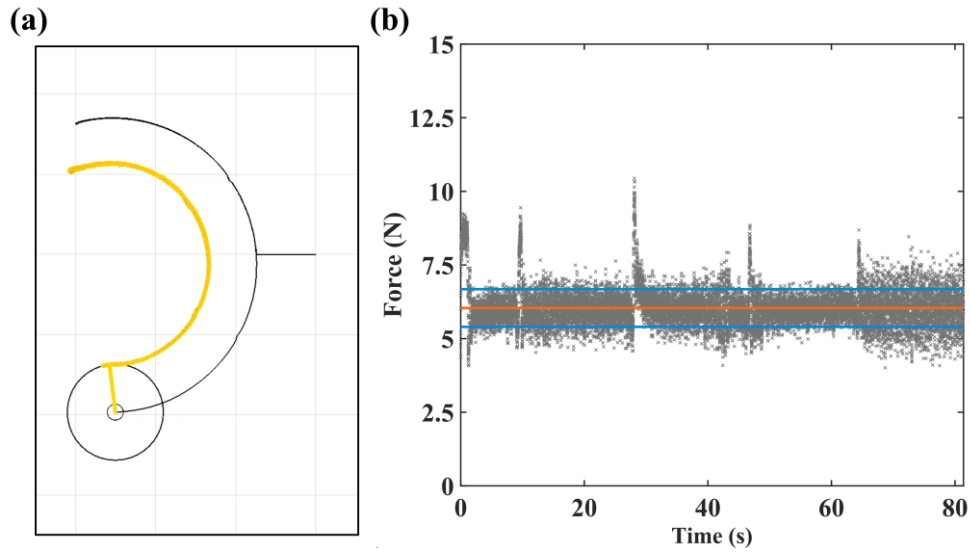

Figure 18. Object manipulation results through force control by autonomous robot control. (a) Position result. The expression method is the same as Figure 13-a. (b) Force result when the forces are applied the robotic skin. The expression method is the same as Figure 13-b.

Chapter 6. Discussion

The main contribution of this work is the modular design of optically sensorized robotic skin that can not only detect the location but also measure the force of a contact. Each skin module has three DoFs for estimating three values, the contact locations in x and y axes and the magnitude of the contact force. The modular design makes the skin system easily reconfigurable and resizable to fit various host structures.

Another contribution is that the sensor data can be quickly processed in real-time. We developed models based on the force and the moment equilibriums, and the geometric constraints, and optimized only for specific constant values where errors are expected. Since only the modeling and optimized constant values are used for the sensor data processing, the processing speed is fast, which enables real-time processing of sensor data in multiple robot environments.

The robotic skin has room for improvement. The estimation error exists in the skin module. When the external force disappears, the joint layer should return to the initial position by elasticity of the wave springs in the S-L joints and the beams. However, the layer does not completely return to the initial position due to friction. This friction occurs between the bead and the bolt of the S-L joint, and also between the bead and the socket in the joint layer. In order to minimize the effect of friction, we lubricated the surfaces of the beads, the sockets in the joint layer, and the bolts of the S-L joints. In addition, the position of the wave spring affected return of the joint layer, since the wave springs provide elasticity for returning to the

original position. Although the wave springs were placed as far as possible from the center in our design, it was impossible to completely eliminate the friction. The RMSE in estimating locations in a low force range is relatively large, since it was hard to return to the original position when a small force was applied due to the friction. Our future work is to minimize the impact of frictions by designing one body with structural three DoFs.

The other improvement can be made by estimating the direction of the contact force if additional DoFs can be added to the current design. Detection of shear force in addition to normal force will enable more sophisticated manipulation of a robot.

Chapter 7. Conclusion

We developed robotic skin with modular design that can detect contact force and its location using embedded FBG strain sensors. The FBG sensor not only enables precise sensing but also is immune to electromagnetic noise, which makes the proposed skin highly useful in harsh environments, such as EMI and radioactive surroundings. The application experiments successfully demonstrated the performance of the proposed robotic skin for remote manipulation and autonomous control or robots.

Chapter 8. Appendix

8.1. Beam Deflection

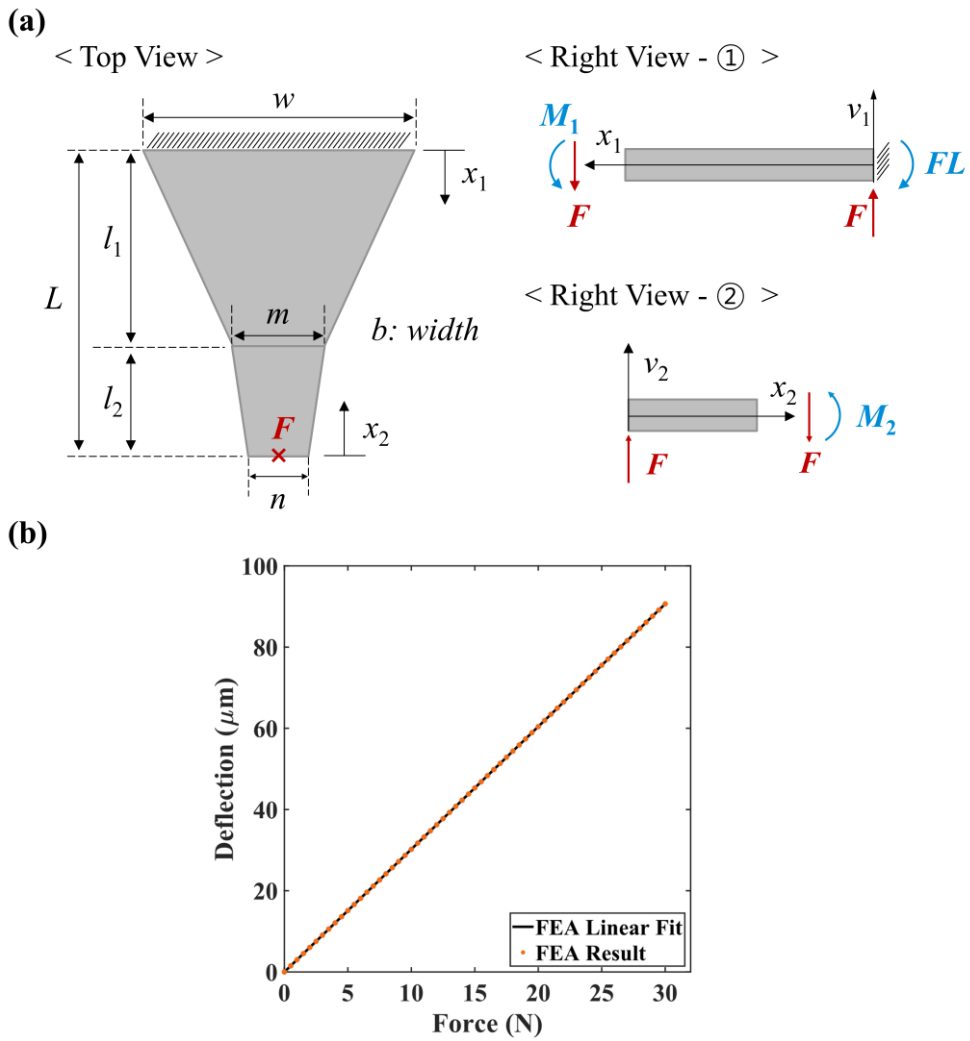

Figure 19. (a) Model of the tapered beam. The right view ① is right side of the beam for x_1, and the right view ② is right side of the beam for x_2. (b) Graph of the deflection for the force using FEA. The deflection is proportional to the force.

Figure 19−a shows constants, variables, and conditions for the beam location estimation. The force, F, is applied to the tip of the beam, and the beam surface at $x_1 = 0$ is fixed. The length constrains are always satisfied as follows

$$x_1 + x_2 = l_1 + l_2 = L\,. \tag{22}$$

Because the width is linearly changed, the width can be given as

$$b = \begin{cases} \frac{w}{L}(L - x_1), & if\ 0 \le x_1 \le l_1 \\ \frac{m-n}{l_2}x_2 + n, & if\ 0 \le x_2 \le l_2 \end{cases}. \tag{23}$$

When x_1 is larger than 0 and smaller than l_1, the moment of inertia and moment are expressed as

$$I_1 = \frac{wh^3(L - x_1)}{12L}, \qquad M_1 = F(L - x_1)\,. \tag{24}$$

The second derivative of v_1 is as follows [43]

$$\frac{d^2v_1}{dx_1^2} = \frac{M_1}{EI_1} = \frac{12L}{Ewh^3}F\,. \tag{25}$$

This equation can be integrated for x_1, and applied the boundary condition at $x_1 = 0$ as follows

$$\begin{gathered} \frac{dv_1}{dx_1} = \frac{12L}{Ewh^3}Fx_1 + C_1 = \frac{12L}{Ewh^3}Fx_1\,, \\ \left(\because dv_1/dx_1|_{x_1=0} = 0\right) \\ v_1 = \frac{6L}{Ewh^3}Fx_1^2 + C_2 = \frac{6L}{Ewh^3}Fx_1^2\,. \\ \left(\because v_1|_{x_1=0} = 0\right) \end{gathered} \tag{26}$$

Thus, $\frac{dv_1}{dx_1}$ and v_1 at $x_1 = l_1$ are given as

$$\begin{aligned} \left.\frac{dv_1}{dx_1}\right|_{x_1=l_1} &= \frac{12L}{Ewh^3}Fl_1 = \frac{V_1}{E}F\,, \\ v_1|_{x_1=l_1} &= \frac{6L}{Ewh^3}Fl_1^2 = \frac{V_2}{E}F \end{aligned} \tag{27}$$

where V_1 and V_2 are constants of l_1, L, w, and h.

When x_2 is larger than 0 and smaller than l_2, the moment of inertia and moment are expressed as

$$I_2 = \frac{h^3}{12}\left(\frac{m-n}{l_2}x_2 + n\right), \qquad M_2 = -Fx_2\,. \tag{28}$$

The second derivative of v_2 is as follows

$$\frac{d^2v_2}{dx_2^2} = \frac{M_2}{EI_2} = -\frac{12l_2x_2}{h^3\left((m-n)x_2 + nl_2\right)}\frac{F}{E} = -\frac{f''(x_2)}{E}F \tag{29}$$

where $f''(x_2)$ is function of l_2, h, m, n, and x_2.

$x_1 = l_1$ is equal location to $x_2 = l_2$. Consequently, Equation (29) can be integrated for x_2, and applies the boundary condition at $x_2 = l_2$ as follows

$$\begin{aligned}
\frac{dv_2}{dx_2} &= -\frac{f'(x_2)}{E}F + C_3 = (-f'(x_2) + f'(l_2) + V_1)\frac{F}{E}, \\
&\qquad \left(\because dv_2/dx_2|_{x_2=l_2} = dv_1/dx_1|_{x_1=l_1}\right) \\
v_2 &= (-f(x_2) + f'(l_2)x_2 + V_1x_2)\frac{F}{E} + C_4 \\
&= [-f(x_2) + (f'(l_2) + V_1)(x_2 - l_2) + f(l_2) + V_2]\frac{F}{E}. \\
&\qquad \left(\because v_2|_{x_2=l_2} = v_1|_{x_1=l_1}\right)
\end{aligned} \tag{30}$$

If we apply $x_2 = 0$, we can get the deflection at the tip as follows

$$v_2|_{x_2=0} = [-f(0) - (f'(l_2) + V_1)l_2 + f(l_2) + V_2]\frac{F}{E} = K_vF \tag{31}$$

where K_v is the deflection proportional constant. Since the deflection at $x_2 = 0$ is proportional to F, the location of the beam forces can be determined by the magnitude of the force. This linearity is also verified by the FEA as shown in Figure 19−b.

Bibliography

[1] M. Spenko, S. Buerger, and K. Iagnemma, The DARPA Robotics Challenge Finals: Humanoid Robots To The Rescue. Cham, Switzerland: Springer International Publishing, 2018.

[2] L. Penco, N. Scianca, V. Modugno, L. Lanari, G. Oriolo, and S. Ivaldi, "A multimode teleoperation framework for humanoid loco-manipulation: An application for the icub robot," IEEE Robotics and Automation Magazine, vol. 26, no. 4, pp. 73–82, 2019.

[3] C. Wong, E. Yang, X. Yan, and D. Gu, "An overview of robotics and autonomous systems for harsh environments," in 2017 23rd International Conference on Automation and Computing (ICAC), 2017, pp. 1–6.

[4] N. Marturi, A. Rastegarpanah, C. Takahashi, M. Adjigble, R. Stolkin, S. Zurek, M. Kopicki, M. Talha, J. A. Kuo, and Y. Bekiroglu, "Towards advanced robotic manipulation for nuclear decommissioning: A pilot study on tele-operation and autonomy," in 2016 International Conference on Robotics and Automation for Humanitarian Applications (RAHA). IEEE, 2016, pp. 1–8.

[5] J. Ramos, A. Wang, and S. Kim, "Robot-human balance state transfer during full-body humanoid teleoperation using divergent component of motion dynamics," in 2016 IEEE International Conference on Robotics and Automation (ICRA). IEEE, 2016, pp. 1587–1592.

[6] F. Abi-Farrajl, B. Henze, A. Werner, M. Panzirsch, C. Ott, and M. A. Roa, "Humanoid teleoperation using task-relevant haptic feedback," in 2018 IEEE/RSJ International Conference on Intelligent Robots and Systems (IROS). IEEE, 2018, pp. 5010–5017.

[7] J. Kofman, X. Wu, T. J. Luu, and S. Verma, "Teleoperation of a robot manipulator using a vision-based human-robot interface," IEEE Transactions on Industrial Electronics, vol. 52, no. 5, pp. 1206–1219, 2005.

[8] Y.-L. Park, S. C. Ryu, R. J. Black, K. K. Chau, B. Moslehi, and M. R. Cutkosky, "Exoskeletal force sensing end-effectors with embedded optical fiber bragg grating sensors," IEEE Transactions on Robotics, vol. 25, no. 6, pp. 1319–1331, 2009.

[9] C. Fox, M. Evans, M. Pearson, and T. Prescott, "Tactile slam with a biomimetic whiskered robot," in 2012 IEEE International Conference on Robotics and Automation (ICRA). IEEE, 2012, pp. 4925–4930.

[10] F. Mazzini and S. Dubowsky, "An experimental validation of robotic tactile mapping in harsh environments such as deep sea oil well sites," in Experimental Robotics: The 12th International Symposium on Experimental Robotics, O. Khatib, V. Kumar, and G. Sukhatme, Eds. Berlin/Heidelberg, Germany: Springer, 2014, pp. 557–570.

[11] M. Lee and H. Nicholls, “Review article tactile sensing for mechatronics—a state of the art survey,” Mechatronics, vol. 9, no. 1, pp. 1–31, 1999.

[12] R. S. Dahiya, G. Metta, M. Valle, and G. Sandini, “Tactile sensing—from humans to humanoids,” IEEE Transactions on Robotics, vol. 26, no. 1, pp. 1–20, 2010.

[13] A. Schmitz, P. Maiolino, M. Maggiali, L. Natale, G. Cannata, and G. Metta, “Methods and technologies for the implementation of large-scale robot tactile sensors,” IEEE Transactions on Robotics, vol. 27, no. 3, pp. 389–400, 2011.

[14] P. Mittendorfer and G. Cheng, “Humanoid multimodal tactile-sensing modules,” IEEE Transactions on Robotics, vol. 27, no. 3, pp. 401–410, 2011.

[15] Z. Kappassov, J.-A. Corrales, and V. Perdereau, “Robotics and autonomous systems,” IEEE Transactions on Industrial Electronics, vol. 74, no. 5, pp. 195–220, 2015.

[16] B. Zhang, J. Wang, G. Q. Zhang, S. Choi, R. Boca, T. A. Fuhlbrigge, and T. Groth, “Teleoperation of machines having at least one actuated mechanism and a fault detection and recovery system,” U.S. Patent 9 682 480, 2017.

[17] J. I. Kim, D. Kim, M. Krebs, Y. S. Park, and Y.-L. Park, "Force sensitive robotic end-effector using embedded fiber optics and deep learning characterization for dexterous remote manipulation," IEEE Robotics and Automation Letters, vol. 4, no. 4, pp. 3481–3488, 2019.

[18] J. P. Clark, G. Lentini, F. Barontini, M. G. Catalano, M. Bianchi, and M. K. O'Malley, "On the role of wearable haptics for force feedback in teleimpedance control for dual-arm robotic teleoperation," in 2019 International Conference on Robotics and Automation (ICRA). IEEE, 2019, pp. 5187–5193.

[19] E. Aranda-Michel, J. Yi, J. Wirekoh, N. Kumar, C. N. Riviere, D. S. Schwartzman, and Y.-L. Park, "Miniaturized robotic end-effector with piezoelectric actuation and fiber optic sensing for minimally invasive cardiac procedures," IEEE Sensors Journal, vol. 18, no. 12, pp. 4961–4968, 2018.

[20] V. J. Lumelsky and E. Cheung, "Real-time collision avoidance in teleoperated whole-sensitive robot arm manipulators," IEEE Transactions on Systems, Man, and Cybernetics, vol. 23, no. 1, pp. 194–203, 1993.

[21] N. F. Lepora, K. Aquilina, and L. Cramphorn, "Exploratory tactile servoing with active touch," IEEE Robotics and Automation Letters, vol. 2, no. 2, pp. 1156–1163, 2017.

[22] U. Martinez-Hernandez, T. J. Dodd, M. H. Evans, T. J. Prescott, and N. F. Lepora, "Active sensorimotor control for tactile exploration," Robotics and Autonomous Systems, vol. 87, pp. 15–27, 2017.

[23] V. Pruks, K. Lee, and J. Ryu, “Shared teleoperation for nuclear plant robotics using interactive virtual guidance generation and shared autonomy approaches,” in 2018 15th International Conference on Ubiquitous Robots (UR). IEEE, 2018, pp. 91–95.

[24] D. Hughes, J. Lammie, and N. Correll, “A robotic skin for collision avoidance and affective touch recognition,” IEEE Robotics and Automation Letters, vol. 3, no. 3, pp. 1386–1393, 2018.

[25] L. Jiang, K. Low, J. Costa, R. J. Black, and Y.−L. Park, “Fiber optically sensorized multi−fingered robotic hand,” in 2015 IEEE/RSJ International Conference on Intelligent Robots and Systems (IROS). IEEE, 2015, pp. 1763–1768.

[26] J.−S. Heo, J.−H. Chung, and J.−J. Lee, “Tactile sensor arrays using fiber bragg grating sensors,” Sensors and Actuators A: Physical, vol. 126, no. 2, pp. 312–327, 2006.

[27] K. O. Hill and G. Meltz, “Fiber bragg grating technology fundamentals and overview,” Journal of Lightwave Technology, vol. 15, no. 8, pp. 1263–1276, 1997.

[28] A. D. Kersey, M. A. Davis, H. J. Patrick, M. LeBlanc, K. P. Koo, C. G. Askins, M. A. Putnam, and E. J. Friebele, “Fiber grating sensors,” Journal of Lightwave Technology, vol. 15, no. 8, pp. 1442–1463, 1997.

[29] W. Zhou, X. Dong, K. Ni, C. Chan, and P. Shum, “Temperature−insensitive accelerometer based on a strain−chirped fbg,” Sensors and Actuators A: Physical, vol. 157, no. 1, pp. 15–18, 2017.

[30] A. Mohammed and S. Djurović, “Fbg thermal sensing features for hot spot monitoring in random wound electric machine coils,” IEEE Sensors Journal, vol. 17, no. 10, pp. 3058–3067, 2017.

[31] Y.-L. Park, S. Elayaperumal, B. Daniel, S. C. Ryu, M. Shin, J. Savall, R. J. Black, B. Moslehi, and M. R. Cutkosky, “Real-time estimation of 3-d needle shape and deflection for mri-guided interventions,” IEEE/ASME Transactions on Mechatronics, vol. 15, no. 6, pp. 906–915, 2010.

[32] W. W. Morey, J. R. Dunphy, and G. Meltz, “Multiplexing fiber bragg grating sensors,” Fiber and Integrated Optics, vol. 10, no. 4, pp. 351–360, 1991.

[33] A. D. Kersey, T. A. Berkoff, and W. W. Morey, “Multiplexed fiber bragg grating strain-sensor system with a fiber fabry-perot wavelength filter,” Optics Letters, vol. 18, no. 16, pp. 1370–1372, 1993.

[34] P. K. C. Chan, W. Jin, and M. Suleyman Demokan, “Fmcw multiplexing of fiber bragg grating sensors,” IEEE Journal of Selected Topics in Quantum Electronics, vol. 6, no. 5, pp. 756–763, 2000.

[35] K. d. M. Sousa, A. A. Hafner, H. J. Kalinowski, and J. C. C. da Silva, “Determination of temperature dynamics and mechanical and stator losses relationships in a three-phase induction motor using fiber bragg grating sensors,” IEEE Sensors Journal, vol. 12, no. 10, pp. 3054–3061, 2012.

[36] J. Hu, Z. Chen, and C. Yu, “150−km long distance fbg temperature and vibration sensor system based on stimulated raman amplification,” Journal of Lightwave Technology, vol. 30, no. 8, pp. 1237–1243, 2012.

[37] Y. Ohmura, Y. Kuniyoshi, and A. Nagakubo, “Conformable and scalable tactile sensor skin for curved surfaces,” in Proceedings of the 2006 IEEE International Conference on Robotics and Automation (ICRA). IEEE, 2006, pp. 1348–1353.

[38] E. del Sol, R. King, R. Scott, and M. Ferre, “External force estimation for teleoperation based on proprioceptive sensors,” International Journal of Advanced Robotic Systems, vol. 11, no. 3, p. 53, 2014.

[39] A. Wahrburg, E. Morara, G. Cesari, B. Matthias, and H. Ding, “Cartesian contact force estimation for robotic manipulators using kalman filters and the generalized momentum,” in 2015 IEEE International Conference on Automation Science and Engineering (CASE). IEEE, 2015, pp. 1230–1235.

[40] L. D. Phong, J. Choi, and S. Kang, “External force estimation using joint torque sensors for a robot manipulator,” in 2012 IEEE International Conference on Robotics and Automation. IEEE, 2012, pp. 4507–4512.

[41] K. O. Hill and G. Meltz, “Fiber bragg grating technology fundamentals and overview,” Journal of Lightwave Technology, vol. 15, no. 8, pp. 1263–1276, 1997.

[42] A. G. Leal−Junior, A. Theodosiou, C. Marques, M. J. Pontes, K. Kalli, and A. Frizera, “Compensation method for temperature cross−sensitivity in transverse force applications with fbg sensors in pofs,” Journal of Lightwave Technology, vol. 36, no. 17, pp. 3660–3665, 2018.

[43] R. C. Hibbeler, Mechanics of Materials, 8th ed. Upper Saddle River, NJ, USA: Pearson Prentice Hall, 2011.

[44] A. Rajabzadeh, R. Heusdens, R. C. Hendriks, and R. M. Groves, “Calculation of the mean strain of smooth non−uniform strain fields using conventional fbg sensors,” Journal of Lightwave Technology, vol. 36, no. 17, pp. 3716–3725, 2018.

[45] H. Seraji, “Adaptive admittance control: an approach to explicit force control in compliant motion,” in Proceedings of the 1994 IEEE International Conference on Robotics and Automation (ICRA), vol. 4. IEEE, 1994, pp. 2705–2712.

Abstract

로봇은 인간과 같은 높은 조작성이 필요한 어려운 작업 환경이나 위험한 환경에서 인간을 대체할 수 있도록 연구되고 있다. 이를 위해 동물의 기계적 감응(mechanoreception) 역할과 같은 기능을 수행하면서 로봇에 부착될 수 있는 스킨을 연구하고 있고, 민감한 로봇 스킨이 부착된 로봇은 높은 수준의 조작성을 가지고 주어진 작업을 성공할 수 있다. 다시 말해 로봇의 힘 센싱과 촉각 센싱 기능은 정교한 로봇 조작의 핵심 요소들 중 하나로 로봇의 세밀한 작업들을 수행하기 필요로 하다. 따라서 우리는 이 연구에서 외부 접촉의 위치뿐만 아니라 외력의 크기도 추정할 수 있는 모듈화된 로봇 스킨을 제안한다. 접촉 힘의 크기, 접촉의 수직 및 수평 위치 등 접촉에 대한 3가지 정보를 얻기 위해서 각 스킨 모듈은 3 자유도를 가지도록 설계하였다. 제안한 스킨에서 힘 센싱은 새롭게 설계한 삼각형 형태의 빔 구조의 변형을 통해서 측정한다. 구체적으로 스킨 모듈의 외피에 가해진 힘은 빔 구조로 전달되고, 이로 인해 발생하는 빔 구조의 변형은 “fiber Bragg gratings” 이라고 불리는 광섬유 스트레인 센서들에 의해서 측정된다. 제안한 스킨은 1.45 N의 힘 추정 해상도를 가지고, 수평 및 수직 위치 추정은 각각 1.85 mm와 1.91 mm의 해상도를 가진다. 우리는 상용화된 로봇팔에 여러 개의 스킨 모듈을 배열 및 부착하여 로봇의 원격 조작 및 무인 조작을 실행하였고, 스킨의 활용성을 검증하였다.